J Adv Ceram

Research Article

Defect-engineering-driven synergistic modulation of dual-phase $(Fe_{0.5}Mg_{0.5}CoNiCuMn)_3O_4$@CuO ceramics for superior microwave absorption

Xia Feng[1,2], Yixiang Lu[1,2], Fanqi Meng[1,2], Yi Hou[1,2,✉], Xiaodong Feng[1,2], Haikui Zhu[1,2], Lixi Wang[1,2,✉]

Cite this article: Feng X, Lu Y, Meng F, et al. *J Adv Ceram* 2026, **15**(2): 9221229. https://doi.org/10.26599/JAC.2025.9221229

ABSTRACT: To overcome the challenge of insufficient loss strength in single-phase high-entropy ferrites, this work develops a novel defect-engineering-driven dual-phase strategy to fabricate spinel/rock-salt structured $(Fe_{0.5}Mg_{0.5}CoNiCuMn)_3O_4$@CuO composite ceramics. The combination of experimental characterization and first-principles calculations demonstrates a strong positive correlation between the defect concentration and microwave absorption performance. The optimized material achieves outstanding electromagnetic absorption with a minimum reflection loss of −48 dB and an effective absorption bandwidth of 3.9 GHz in the X-band. Remarkably, this work obtains 70% bandwidth retention after oxidation at 1200 °C and a thermal conductivity of 2.154 $W \cdot m^{-1} \cdot K^{-1}$, demonstrating exceptional high-temperature stability and thermal management capability. This study pioneers a new pathway for the development of oxidation-resistant and electromagnetic protection materials through defect-engineering-driven synergistic modulation.

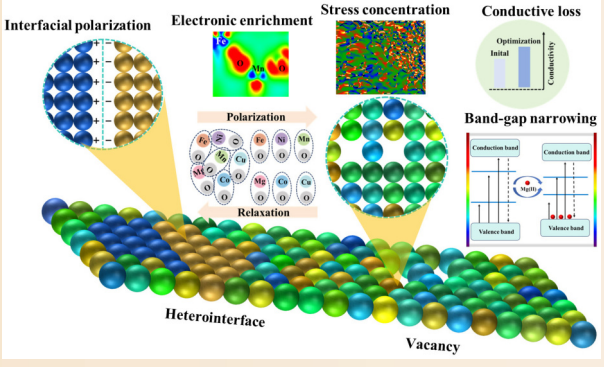

KEYWORDS: high-entropy ferrite ceramics; defect engineering; lattice distortion; surface oxygen vacancy; electromagnetic protection

1 Introduction

With the rapid advancement of modern communication technologies, electromagnetic pollution has become increasingly severe, posing potential threats to both the environment and human health [1–4]. The development of electromagnetic wave-absorbing materials characterized by thinness, high efficiency, light weight, and broad absorption bandwidth has emerged as a critical direction to address this challenge [5,6]. Currently, widely studied absorbers mainly include dielectric loss materials such as silicon carbide and conducting polymers, as well as magnetic loss materials such as ferrites [7]. Through elemental doping and structural design, synergistic regulation of dielectric and magnetic losses has been achieved to some extent [8]. Although these materials exhibit relatively good absorption performance, significant challenges remain in terms of precise microstructural control, effective utilization of interface effects, and the complexity of preparation processes [9]. Furthermore, with the growing demand for applications in extreme environments, traditional electromagnetic absorbers are also required to possess comprehensive properties such as excellent thermal stability and high-temperature oxidation resistance [10,11].

High-entropy ceramics are a class of inorganic compounds formed by solid solutions of five or more principal elements in near-equimolar ratios [12,13]. The diverse compositional designs and tunable structural characteristics of these materials demonstrate broad application prospects in the field of electromagnetic wave absorption. Reported systems such as high-entropy carbide, boride, and oxide ceramics have all shown good impedance matching performance [14,15]. Owing to their unique high-entropy effects, these ceramics combine excellent thermal stability with relatively high thermal conductivity, making them particularly suitable for extreme environment applications [10]. As an important category of high-entropy oxide ceramics, high-entropy ferrite ceramics can induce valence band compensation effects through disordered multivalent cation arrangements, thereby regulating the defect concentration, band structure, and chemical disorder, which effectively tunes the electrical conductivity and enhances the dielectric properties. Moreover, the incorporation of magnetic ions in high-entropy ferrite ceramics

[1] College of Materials Science and Engineering, Nanjing Tech University, Nanjing 211816, China. [2] Jiangsu Collaborative Innovation Center for Advanced Inorganic Function Composites, Nanjing 211816, China.

✉ Corresponding authors. E-mail: Y. Hou, houyi@njtech.edu.cn; L. Wang, wanglixi_njut@163.com

Received: September 9, 2025; Revised: November 14, 2025; Accepted: December 9, 2025

can strengthen ferromagnetic coupling, further improving the magnetic loss capability. In recent years, high-entropy ferrite ceramics, such as $(Mn_{0.2}Co_{0.2}Cu_{0.2}Zn_{0.2}Mo_{0.2})Fe_2O_4$ and MFe_2O_4 (M = Mg, Mn, Fe, Co, Ni, Cu, Zn), have been demonstrated to exhibit outstanding microwave absorption performance [16,17].

However, single-phase high-entropy ferrite ceramics still face limitations such as poor impedance matching, often necessitating the introduction of a second phase to construct composite structures to optimize impedance matching and enhance interface polarization effects [18,19]. For example, compounding high-entropy ferrite ceramics with highly conductive materials can effectively modulate their dominant loss mechanism [20]. Furthermore, during the formation of multiphase structures, various defects (e.g., point defects, dislocations, and interface disorder) and stress-induced effects are readily generated within high-entropy ferrite ceramics [21–23]. These defects act as a double-edged sword: For example, surface oxygen vacancies form more readily under thermodynamic conditions in high-entropy oxides and can be intentionally introduced to enhance the dielectric response by increasing the free carrier concentration or by acting as polarization centers [14,24]; however, randomly distributed or excessively high concentrations of defects can also lead to disordered electromagnetic parameters and impedance mismatch, thereby reducing the wave-absorbing performance [25,26]. Therefore, precise regulation of the defect concentration and spatial distribution is crucial for achieving synergistic optimization of impedance matching and loss mechanisms.

On the basis of defect-engineering-driven synergistic modulation, this study successfully prepared composite ceramics of high-entropy ferrite ($(Fe_{0.5}Mg_{0.5}CoNiCuMn)_3O_4$) and copper oxide (CuO) through precise compositional design, achieving controllable construction of a defect gradient. Combining first-principles calculations with experimental validation, a positive correlation between the defect concentration and microwave absorption performance was established. Under conditions of a lattice distortion rate of 0.86% and an interface oxygen vacancy (V_{OS}) concentration of 51.89%, the material exhibited optimal impedance matching behavior. The optimized composite ceramics demonstrated excellent microwave absorption performance: a minimum reflection loss (RL_{min}) of −48 dB and a maximum effective absorption bandwidth (EAB_{max}) of 3.9 GHz, outperforming most reported ceramic-based absorbers. After high-temperature oxidation at 1200 °C, the electromagnetic absorption performance decreased by only approximately 30% (EAB_{max} = 2.7 GHz), indicating good oxidation resistance. Thermal conductivity measurements revealed a thermal conductivity of up to 2.154 $W \cdot m^{-1} \cdot K^{-1}$, suggesting potential applicability in thermal management scenarios. This study provides new insights and a theoretical basis for the design and optimization of high-temperature oxidation-resistant and high-performance electromagnetic absorbing materials intended for extreme environments.

2 Experimental

2.1 Material preparation

$(Fe_{0.5}Mg_{0.5}CoNiCuMn)_3O_4$@CuO were synthesized via a solid-state reaction using Fe_2O_3, MgO, CoO, NiO, CuO, and MnO_2 as raw materials. All the metal oxide powders, with purities greater than 99.9%, are supplied by Aladdin. The raw materials are accurately weighed according to their stoichiometric ratios and mixed with an appropriate amount of ethanol in a zirconia ball-milling jar. The mixture was ball-milled for 12 h to ensure homogeneity. The resulting slurry was dried at 60 °C for 8 h to remove ethanol. The dried powders were further ground using a mortar and sieved through a 120-mesh screen to obtain black high-entropy ceramic powders. These powders are then uniaxially pressed into black blocks with dimensions of 5 mm × 10 mm under a pressure of 10 MPa. Finally, the blocks were sintered in air using a muffle furnace. The sintering procedure was as follows: The samples were heated from room temperature to 1000 °C at a rate of 5 $°C \cdot min^{-1}$, further heated to the final sintering temperatures (ranging from 800 to 1300 °C) at a slower rate of 2.5 $°C \cdot min^{-1}$, held at the final sintering temperature for 4 h, and then allowed to cool naturally to room temperature inside the furnace. This process yielded dual-phase high-entropy ferrite ceramics $(FeCoNiCuMn)_3O_4$ and CuO, designated Mg-1. Similarly, $(Fe_{0.75}Mg_{0.25}CoNiCuMn)_3O_4$ and CuO, $(Fe_{0.5}Mg_{0.5}CoNiCuMn)_3O_4$ and CuO, $(Fe_{0.25}Mg_{0.75}CoNiCuMn)_3O_4$ and CuO, and $(MgCoNiCuMn)_3O_4$ and CuO are synthesized and designated Mg-2, Mg-3, Mg-4, and Mg-5, respectively.

2.2 Characterizations

The phase composition and structural evolution of the samples are characterized using an X-ray diffractometer (XRD; Ultima IV) with Rietveld refinement. Microstructural features and elemental distributions are analyzed by a field-emission scanning electron microscope (FE-SEM; HITACHI SU8010). High-resolution microstructure observations are performed using a transmission electron microscope (TEM; JEM-2100F, JEOL). Elemental valence states and defect characteristics are examined using an X-ray photoelectron spectrometer (XPS; Kratos Axis Ultra DLD AXIS SUPRA). The magnetic hysteresis loops and electrical conductivity are measured using a vibrating sample magnetometer (VSM; LakeShore 7404) and a resistivity meter (ST2253Y, Suzhou Jingge Electronic), respectively. The thermal conductivity was measured by a laser-flash apparatus (LFA 457, NETZSCH) on disk-shaped samples with a diameter of 12.7 mm and a thickness of 3 mm. The high-entropy ferrite ceramics were cut into dimensions of 22.8 mm × 10.1 mm × 2.5 mm, and their complex relative permittivity and permeability were measured using a vector network analyzer (3672B, Ceyear) over the frequency range of 8.2–12.4 GHz.

CST Studio Suite (CST) is employed to simulate the radar cross-section (RCS) of the samples. The samples are modeled as squares with dimensions of 100 mm × 100 mm, comprising a bilayer structure. The top layer consists of high-entropy oxide ceramic material, whereas the bottom layer is a perfect electric conductor (PEC) with a thickness of 1 mm. The simulation frequency range is within the 8.7 GHz regime. The absorption model is positioned on the *X*–O–*Y* plane, with microwaves incident along the negative *Y*-axis and the electric field polarized along the *Z*-axis. The scattering direction is analyzed in terms of the spherical coordinate angles (θ and φ).

Density functional theory (DFT) calculations were carried out with the Vienna *ab initio* simulation package (VASP). The exchange–correlation functional was treated within the generalized gradient approximation (GGA) using the Perdew–Burke–Ernzerhof (PBE) formulation. Electron–ion interactions were described using the projector augmented wave (PAW) method, with a plane-wave kinetic energy cutoff set to 400 eV. This cutoff energy and the *k*-point mesh were chosen on the basis of comprehensive convergence tests. A Γ-centered *k*-point grid with dimensions of 4 × 3 × 3 was adopted for Brillouin zone sampling. The unit cell volume was optimized to 407.6215 $Å^3$. During structural relaxation, all the atomic positions were fully

optimized. The convergence thresholds for the self-consistent field iterations were set to 10^{-5} eV for energy and 0.02 eV·Å^{-1} for forces.

3 Results and discussion

3.1 Composition, structure, morphology, and defect engineering design

Figure 1(a) presents the XRD patterns of the Mg-1–5 systems after calcination at 1200 °C for 4 h. All the diffraction peaks perfectly match the spinel structure of Fe_3O_4 (PDF#75-0449) and the rock-salt structure of CuO (PDF#89-5899), confirming that the high-entropy ceramic consists of a two-phase composite ($(Fe_{0.5}Mg_{0.5}CoNiCuMn)_3O_4$ phase and CuO phase), named $(Fe_{0.5}Mg_{0.5}CoNiCuMn)_3O_4$@CuO. Furthermore, to provide additional evidence for the successful synthesis of the high-entropy phase, we performed configurational entropy calculations on the cation sites of $(Fe_{0.5}Mg_{0.5}CoNiCuMn)_3O_4$. According to the configurational entropy formula, the calculated result is 15.93 J·mol^{-1}·K^{-1}. In the field of high-entropy materials, 1.5R (i.e., 1.5×8.314 ≈ 12.47 J·mol^{-1}·K^{-1}) is widely recognized as the criterion threshold. Since 15.93 > 12.47 J·mol^{-1}·K^{-1}, this thermodynamically confirms that the spinel phase itself is a typical high-entropy solid solution. Notably, as the Mg doping concentration increases, the XRD diffraction peaks exhibit a systematic shift toward lower angles [27]. According to Bragg's equation ($2d\sin\theta = n\gamma$), this shift originates from the larger ionic radius of the divalent magnesium ion than the trivalent iron ion, resulting in lattice expansion [27]. To analyze the evolution of the lattice parameters quantitatively, Rietveld refinement is performed on the Mg-1–5 systems (Fig. S1 in the Electronic Supplementary Material (ESM) and Fig. 3(c)). The reliability of the refinement results is well supported by the R_{wp} values, all of which are below 10% [28]. The refined data (Table S1 and Fig. S2 in the ESM) further reveal that with increasing Mg concentration, the unit cell parameters, angles, and unit cell volume of both phases initially increase but then decrease, reaching a peak at Mg-3. The volume of the CuO phase changes little. This observed phenomenon is attributed primarily to the evolution of Mg^{2+} occupation. In the initial stage, Mg^{2+} ions, owing to their strong preference for tetrahedral coordination, preferentially occupy the tetrahedral interstitial sites. The relatively large ionic radius consequently induces lattice expansion. As the Mg content continues to increase to the point where the tetrahedral sites approach saturation, the additional Mg^{2+} ions begin to occupy the octahedral interstitial sites. This process likely involves the displacement of smaller ions. The resulting lattice contraction effect surpasses the expansion effect caused by the ionic radius, thereby leading to a reduction in the unit cell volume. Moreover, the CuO phase essentially maintains constant lattice parameters because of its extremely limited solid solubility for Mg^{2+} within its crystal structure and its stable chemical composition. Although the volume of the copper oxide phase in Mg-5 increases, the overall volume of both phases remains smaller than that of Mg-3. This phenomenon indicates that Mg^{2+}

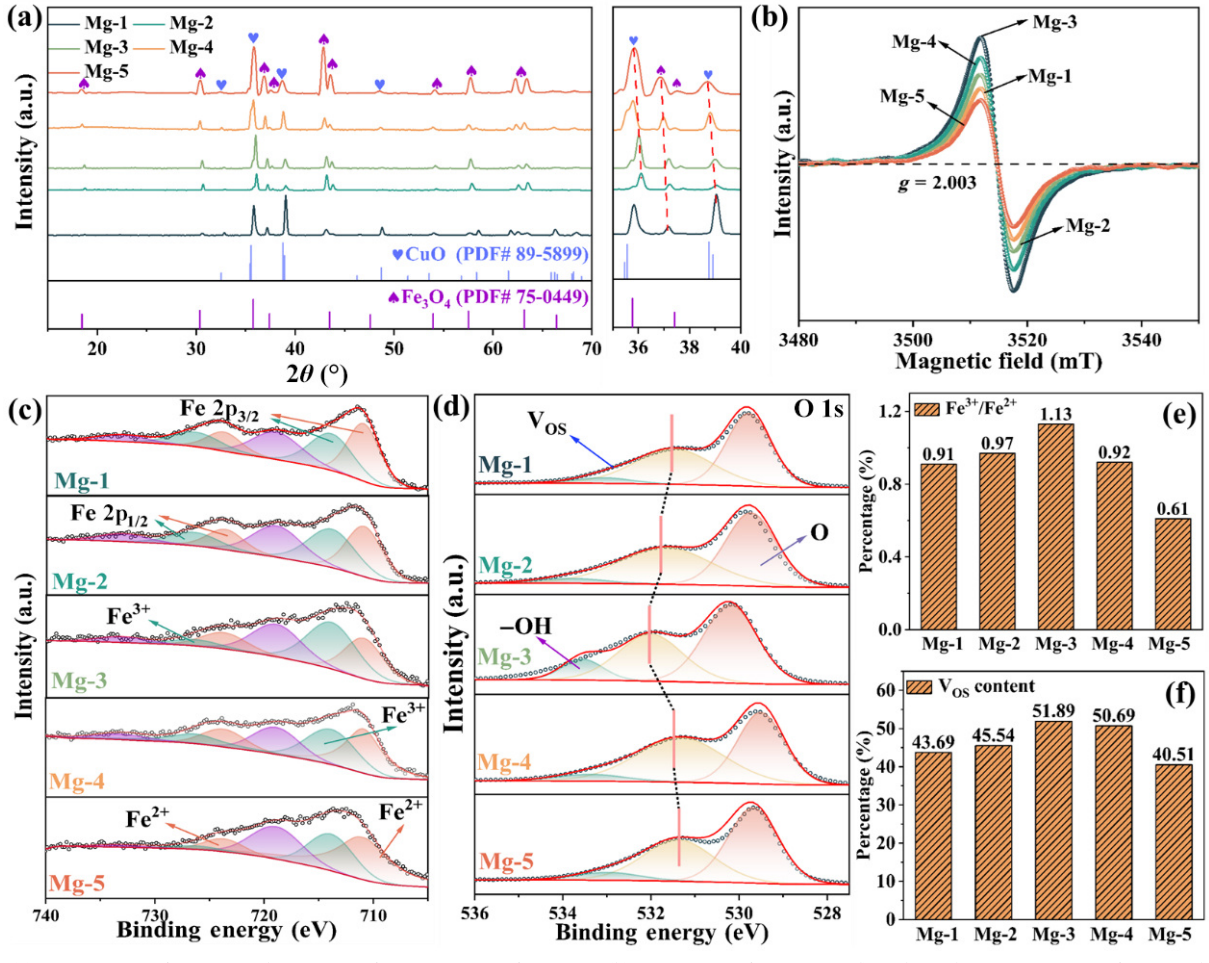

Fig. 1 (a) XRD patterns of Mg-1–5 and XRD magnification patterns of 35.5°–40°. (b) EPR spectra of Mg-1–5. (c, d) High-resolution XPS spectra of Fe 2p and O 1s of Mg-1–5. (e, f) Fe^{3+}/Fe^{2+} and surface V_{OS} contents of Mg-1–5.

清華大学出版社 Tsinghua University Press | SciOpen

substitution not only directly modulates the lattice parameters but also induces lattice distortion due to ionic radius mismatch, thereby providing a structural foundation for the subsequent optimization of electromagnetic properties. Furthermore, Fig. S3 in the ESM compares the XRD patterns of the Mg-3 system with those of typical single-component spinel oxides, confirming its characteristic long-range order and short-range disorder, which are hallmarks of high-entropy ceramics.

XPS was employed to investigate the surface chemical states and electronic structure characteristics of the etched Mg-1–5 samples. The survey spectrum (Fig. S4 in the ESM) reveals the presence of Fe 2p, Co 2p, Ni 2p, Cu 2p, Mn 2p, and Mg 1s characteristic peaks, confirming the synergistic coexistence of Fe, Co, Ni, Cu, Mn, and Mg multimetallic elements. The high-resolution Fe 2p spectrum (Fig. 1(c)) exhibits distinct peaks at binding energies of 713.87, 726.32, 710.89, and 723.72 eV, which correspond to Fe^{3+} and Fe^{2+}, respectively [29]. The coexistence of multiple valence states of Fe suggests strong electronic interactions with neighboring metal cations, a characteristic closely aligned with the structural formation mechanism of high-entropy oxides. Notably, the difference in crystal field stabilization energy drives Fe^{2+} to preferentially occupy octahedral sites, whereas Fe^{3+} is distributed across both tetrahedral and octahedral sites. This disordered cation arrangement induces significant variations in the bonding energy with oxygen ions, which thermodynamically favors the formation of cation vacancies.

In general, the synergistic effect of multiple metal elements significantly enhances the oxidation reaction kinetics, thereby increasing the surface V_{OS} concentration in high-entropy systems. The high-resolution O 1s spectrum (Fig. 1(d)) reveals three characteristic components: lattice oxygen (529.88 eV), V_{OS} (531.21 eV), and surface-adsorbed water (532.82 eV). The V_{OS} is regulated by adjusting the elemental ratios, whereas the variation in surface-adsorbed water originates from lattice distortion extending to the material surface. This leads to irregular atomic arrangements and an increase in unsaturated bonds, thereby resulting in increased surface energy. The elevated surface energy makes the material surface more inclined to adsorb water molecules to reduce its energy and achieve a more stable state. Compared with the other samples, Mg-3 exhibits the most significant lattice distortion, which accounts for its highest amount of surface-adsorbed water molecules. Under an alternating electromagnetic field, the –OH groups, which are strongly polar, undergo directional reorientation, resulting in orientation polarization. Moreover, these polar groups interact with defects such as V_{OS} within the material, forming many dipoles and inducing dipole polarization. The synergistic effect of these multiple polarization mechanisms ultimately influences the wave-absorbing properties. To further determine the relationship between the metal valence state and surface V_{OS} concentration, the ratio of the Fe^{3+}/Fe^{2+} to the surface oxygen defect concentration was estimated by calculating the ratio of the area of the high-binding-energy component associated with the Fe^{3+}/Fe^{2+} and surface oxygen vacancies to the total area, as shown in Figs. 1(e) and 1(f) and Tables S2 and S3 in the ESM. However, the approach provides a relative value intended for trend comparison and inherently involves systematic deviations from the true absolute concentration.

With increasing Mg doping, the Fe^{3+}/Fe^{2+} area ratio exhibits a nonmonotonic trend, initially decreasing but then increasing. Notably, the area ratio of the surface oxygen vacancy characteristic peak exhibits an inverse relationship with the Fe^{3+}/Fe^{2+} ratio, suggesting a significant positive correlation between the increase in surface oxygen vacancy concentration and the relative concentration of Fe^{2+} but a negative correlation with the relative concentration of Fe^{3+}. This correlation can be attributed to the electronic configuration of Fe^{2+}, which is more favorable for surface oxygen vacancy formation, as its unfilled 3d orbitals can stabilize surface oxygen vacancy defects through a charge transfer mechanism. Quantitative XPS analysis reveals that the concentration of surface oxygen vacancies initially increases but then decreases with increasing magnesium doping concentration. Among all the samples, Mg-3 exhibits the highest relative surface oxygen vacancy concentration, reaching a peak value of 51.89%. In addition, the high-resolution XPS spectra of the other elements are presented in Fig. S5 in the ESM.

To further verify the reliability of this result, electron paramagnetic resonance (EPR) spectroscopy was employed to quantitatively characterize the oxygen-related defects. As shown in Fig. 1(b), the *g*-factor (the dimensionless proportionality constant that scales the ratio of the magnetic moment of an unpaired electron to its angular momentum) for all the samples remains constant at 2.003, confirming the presence of oxygen vacancies. Notably, the intensity of the characteristic EPR signal first increases but then decreases with increasing Mg doping, with the Mg-3 sample exhibiting the strongest signal. This indicates that the highest content of surface oxygen vacancies is present in this sample.

Figure 2(a) shows SEM images of the Mg-3 sample after high-temperature calcination. Microstructural analysis reveals significant morphological heterogeneity: The substrate region exhibits a relatively smooth surface, whereas the protruded areas display a strip-like structure, and the average grain size of Mg-3 is 23.87 μm (Fig. S6 in the ESM). Additionally, micron-sized pores are dispersed throughout the base. To evaluate the degree of densification of the samples, the porosity was measured using the Archimede drainage method. As shown in Fig. S7 in the ESM, under the same preparation process, the porosity of the samples increases with increasing Mg concentration, which is accompanied by a corresponding decrease in density. This phenomenon can be primarily attributed to the much higher melting point of magnesium oxide than that of iron oxide. The introduction of a high Fe concentration may facilitate the formation of a certain amount of liquid phase during sintering, significantly enhancing the densification process through a "liquid-phase sintering" effect. In contrast, systems with higher Mg concentrations tend to undergo solid-state sintering, which requires higher temperatures or longer holding times to achieve full densification. Energy-dispersive spectrometer (EDS) mapping analysis further confirms that Fe, Mg, Co, Ni, Cu, and Mn are uniformly distributed within the substrate phase, collectively forming the $(Fe_{0.5}Mg_{0.5}CoNiCuMn)_3O_4$ phase. In contrast, Cu is significantly enriched in the strip-like regions, leading to the formation of a distinct CuO phase. This pronounced microstructural variation provides direct evidence of phase separation among the multicomponent constituents. The mechanism underlying this phenomenon can be attributed to the regulation of the metal element molar ratio, which limits the thermodynamic driving force for the formation of high configurational entropy. When the system possesses sufficient driving force, metal cations undergo entropy-driven cooperative diffusion, leading to the formation of single-phase high-entropy ferrite ceramics. Conversely, under conditions of insufficient driving force, the individual components tend to undergo competitive diffusion, resulting in a multiphase composite structure. This behavior aligns well with classical configurational entropy regulation theory.

TEM characterization (Fig. 2(b)) reveals that the Mg-3

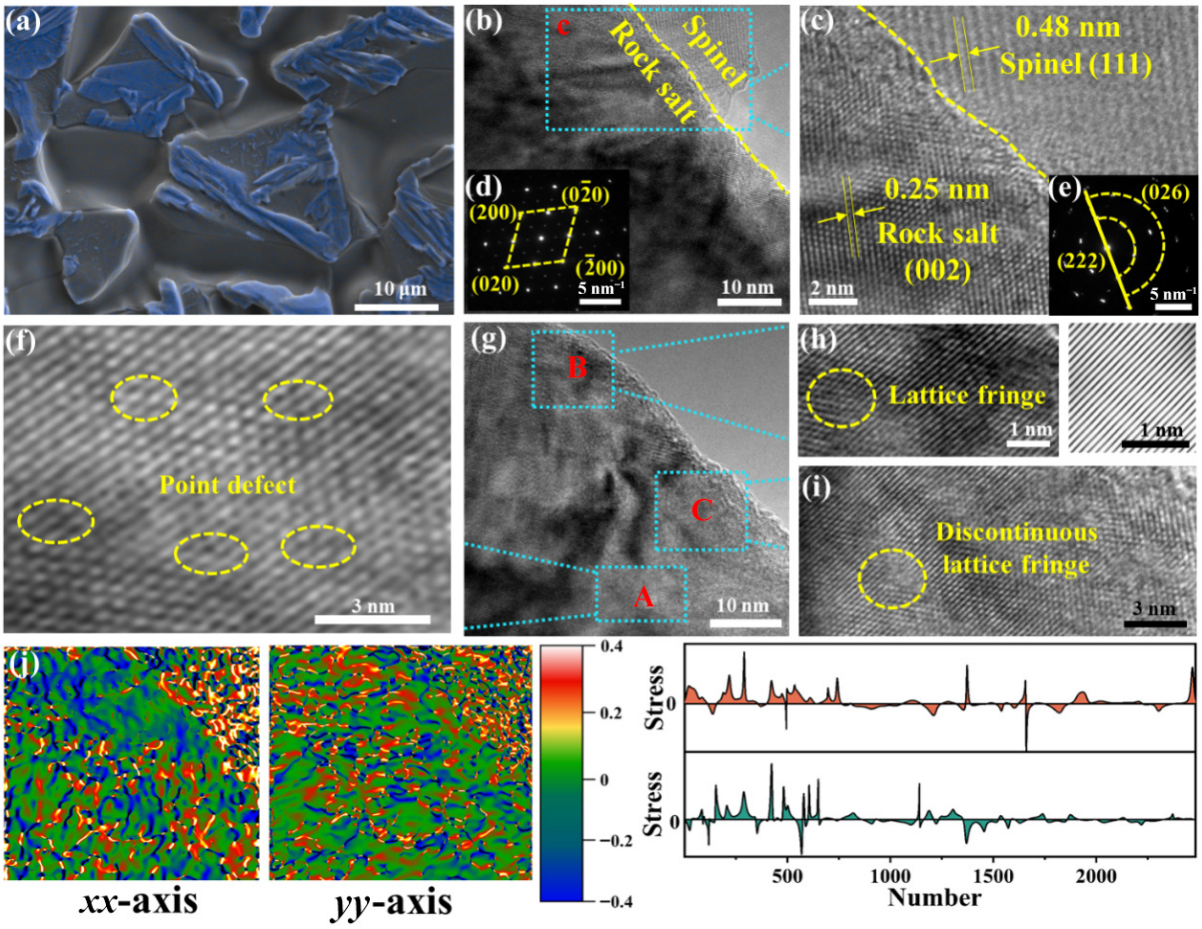

Fig. 2 (a) SEM image and EDS mapping of Mg-3. (b, c, g) HRTEM image. (d, e) SAED patterns of Mg-3. (f, h, i) Enlarged HRTEM images in (g). (j) Stress distribution and statistical curves were obtained by GPA method.

composite primarily consists of a rock-salt-structured CuO phase and a spinel-structured $(Fe_{0.5}Mg_{0.5}CoNiCuMn)_3O_4$ phase. The interface between these two phases is well-defined, exhibiting a distinct grain boundary (Fig. 2(c)). High-resolution TEM (HRTEM) reveals that the characteristic crystal plane spacings of 0.48 and 0.25 nm correspond to the (111) plane of the spinel phase and the (002) plane of the rock-salt phase, respectively. In high-entropy systems, the valence state differences among multiple metal ions lead to the accumulation of lattice distortion energy. To maintain structural stability, $[MO_4]$ tetrahedral and $[MO_6]$ octahedral coordination units undergo cooperative distortion. The selected area electron diffraction (SAED) patterns (Figs. 2(b) and 2(c)) further confirm the coexistence of the two phases. Specifically, the rock-salt phase exhibits a set of diffraction spots forming a parallelogram, attributed to the (200), (0$\bar{2}$0), ($\bar{2}$00), and (020) planes. Moreover, the spinel phase is characterized by diffraction rings corresponding to the (026) and (222) planes. The presence of point defects is definitively established by the variation in cation valence states, direct XPS fitting, and characteristic response in EPR spectra (Figs. 1(b) and 1(d)). These point defects are also manifested in the magnified HRTEM images (Figs. 2(f)–2(i)) as localized contrast variations, which are observed alongside discontinuous lattice fringes [15]. Furthermore, the atomic arrangement along the lattice planes in the yellow-marked region (Fig. 2(g)) clearly reveals pronounced lattice distortions. These findings further verify the presence of abundant structural defects in Mg-3, where strong polarization effects induced by lattice distortions, discontinuous lattice fringes, and point defects contribute to enhanced electromagnetic wave dissipation. The stress distribution and statistical curves along the *xx* and *yy* biaxial directions of the Mg-3 material are quantitatively characterized based on the GPA method (Fig. 2(j)), with a specific focus on the interface between the two phases. The visualized stress field results indicate that the red regions correspond to the tensile stress zone, the blue regions represent the compressive stress zone, and the green regions denote the stress-free area. Notably, a significant stress gradient is observed at the material interface region (upper right quadrant), with the boundary line closely matching the phase interface identified by TEM analysis.

The quantitative statistics further reveal that the $(Fe_{0.5}Mg_{0.5}CoNiCuMn)_3O_4$ phase exhibits a concentrated distribution of tensile stress (high-density red regions), whereas the CuO phase predominantly features compressive stress (high-density blue regions). This pronounced heterogeneity in stress distribution highlights the complex interfacial stress-matching characteristics within the material. In addition, the degree of stress variation in the $(Fe_{0.5}Mg_{0.5}CoNiCuMn)_3O_4$ phase is markedly greater than that in the CuO phase. This significant variation can be attributed to the inherent "lattice distortion effect" of high-entropy systems: The substantial differences in the atomic properties among the multiple metallic cations (Fe/Mg/Co/Ni/Cu/Mn) induce severe lattice distortions when a single-phase solid solution is formed, causing individual atoms to deviate from their original equilibrium positions.

Since the concept of entropy-stabilized oxides was introduced, high-entropy ceramic systems with diverse structures, such as spinel and rock-salt, have undergone significant development [20]. As shown in Fig. 3(a), the spinel structure features a cubic close-

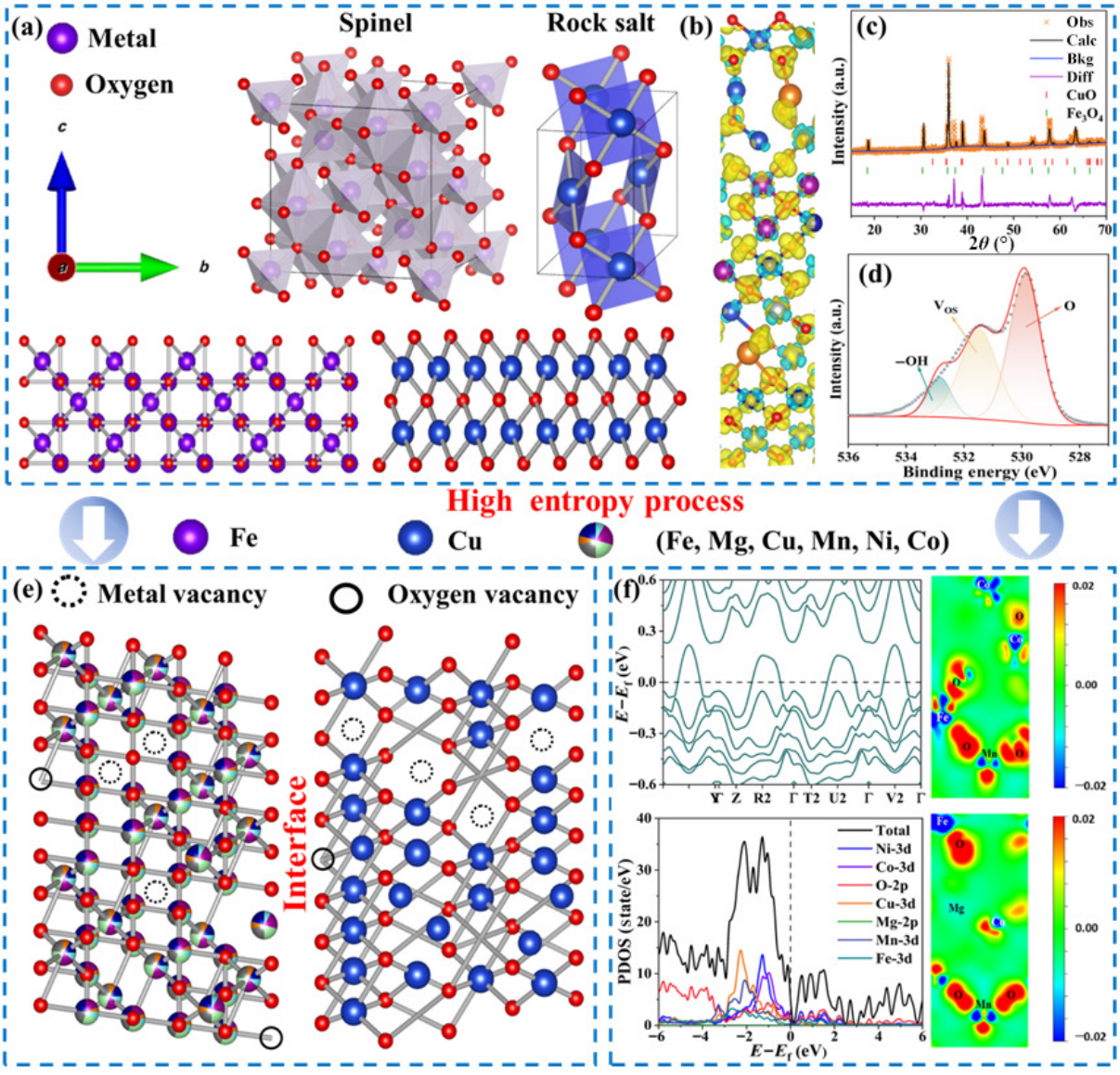

Fig. 3 (a) Crystal structure of spinel and rock-salt phases. (b) CDD plots for Mg-3. (c) XRD refinement pattern for Mg-3. (d) High-resolution O 1s XPS spectra. (e) Diagram of defects, metal vacancies, and oxygen vacancies in Mg-1–5. (f) Band structure, PDOS, and CDD plots for Mg-3.

packed arrangement of oxygen ions, with divalent cations occupying 1/8 of the tetrahedral interstice and trivalent cations filling half of the octahedral interstice. In contrast, the rock-salt structure also maintains a cubic close-packed oxygen sublattice, but all octahedral interstices are fully occupied by smaller cations. Owing to its intricate lattice topology and versatile metal ion coordination, the spinel structure can effectively construct multiple scattering and reflection pathways for electromagnetic wave propagation. Moreover, rock-salt-type high-entropy ceramics, benefiting from their high dielectric constant and magnetic permeability, exhibit excellent impedance matching for electromagnetic wave absorption. In this study, Fe, Co, Ni, Cu, Mn, and Mg are precisely incorporated into the A/B sites of the spinel structure and composited with rock-salt-type CuO to construct a multiphase high-entropy ceramic system (Mg-1–5). This approach successfully establishes the heterointerface shown in Fig. 3(e), leading to outstanding performance in electromagnetic wave absorption.

On the basis of the Rietveld refinement results (Fig. 3(c)), this study quantitatively characterized the degree of lattice distortion using the evolution of the unit cell parameters from Mg-1 to Mg-5 (Table S1 in the ESM), with Mg-1 serving as the initial reference template. The experimental data indicate that, compared with that of the Mg-1 sample, the total volume of Mg-3 increases by 0.86%. Moreover, the abundant defects in high-entropy ceramics facilitate the construction of multiple heterogeneous systems, thereby enabling a multiscale synergistic effect for electromagnetic wave absorption. Specifically, it is widely reported that grain boundary defects primarily enhance high-frequency electromagnetic wave scattering [30], whereas point defects are known to dominate low-frequency energy dissipation via polarization relaxation processes [31]. By precisely controlling the Mg ion concentration, the distribution of surface V_{OS} within the high-entropy structure can be directionally optimized, significantly enhancing the microwave absorbing properties. Fine spectral analysis of the O 1s core level (Fig. 3(d) and Table S3 in the ESM) reveals that the surface V_{OS} concentration initially increases and then decreases with increasing Mg concentration, reaching a peak of 51.89% at Mg-3 before decreasing to 40.54% at Mg-5. The degree of lattice distortion was determined by comparing the volume change of the refined sample with that of Mg-1. On this basis, a defect gradient control system is established, defining a lattice distortion

degree range from −0.15% to 0.86% and a surface V_{OS} concentration modulation range of 40.54%–51.89%.

First-principles calculations were conducted to construct the electronic band structure of Mg-3 (Fig. 3(f)). Band structure analysis reveals a significant overlap between the Fermi level and the conduction band, along with a continuous electronic state distribution near the Fermi surface, confirming the metallic nature and excellent electrical conductivity of Mg-3. First-principles calculations further indicate a dual regulatory mechanism of surface V_{OS} on electrical conductivity: (i) Local electronic enrichment at defect sites significantly increases the carrier concentration, and (ii) band-gap narrowing effectively reduces the electron transition barrier, thereby enhancing conduction loss. Notably, crystal field splitting induces d-orbital reconstruction (t_{2g}–e_g), which significantly enhances the magnetic loss capability by promoting magnetic moment coupling.

Partial density of states (PDOS) analysis reveals that the Fe 3d, Co 3d, Ni 3d, and O 2p orbitals predominantly contribute to the valence band formation of Mg-3. Notably, while the introduction of Mg^{2+} does not induce significant orbital reconstruction, its content gradient increase serves as the primary driver for surface V_{OS} formation, as confirmed by quantitative XPS analysis [12]. Furthermore, the charge density difference (CDD) map (Fig. 3(b)) demonstrates that the constituent cations within the high-entropy ceramic facilitate charge transfer to the oxygen coordination environment, resulting in an asymmetric electron cloud distribution. This charge redistribution effect not only facilitates localized electron accumulation around the surface V_{OS} but also disrupts the lattice symmetry, inducing a high density of dipoles that enable broadband electromagnetic wave absorption.

3.2 Microwave absorption properties at room temperature

On the basis of quarter-wavelength theory, this study systematically investigates the relationship between the matching thickness (t_m) and the matching frequency (f_m) of Mg-3 [32]. Figure 4(a) illustrates the variation in RL_{min} under different thickness conditions. As t_m increases from 2.0 to 2.7 mm, the absorption peak exhibits a systematic shift toward lower frequencies, closely aligning with the predictions of the classical quarter-wavelength theory. This phenomenon arises from the destructive interference between incident and reflected waves at the material interface when the absorber thickness satisfies the quarter-wavelength condition, ultimately minimizing reflection loss. Notably, when t_m is optimized to 2.2 mm, the material achieves an RL_{min} of −48.0 dB at the matching frequency, demonstrating the exceptional electromagnetic wave-absorption performance of Mg-3.

The electromagnetic response mechanism of the Mg-1–5 composite materials is elucidated through an analysis of its electromagnetic parameters (Fig. 4(b)). The experimental results indicate that within the X-band (8.2–12.4 GHz), Mg-1 and Mg-5 exhibit dispersion, with their real permittivity (ε') displaying a

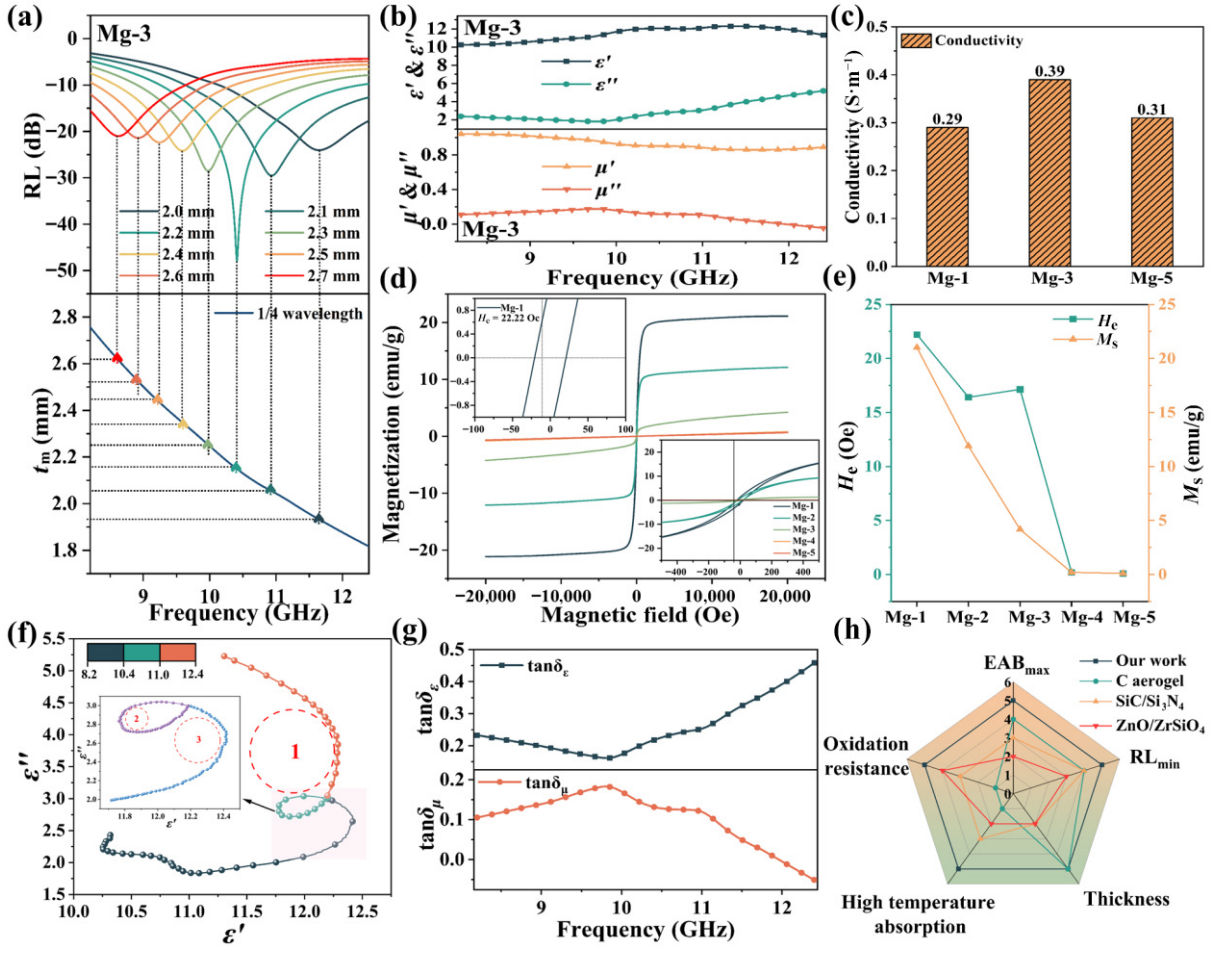

Fig. 4 (a) RL–*f* curves and corresponding quarter-wavelength curves of Mg-3. (b) Real and imaginary parts of complex permittivity and permeability. (c) Electrical conductivity of Mg-1–5. (d) Hysteresis loops of Mg-1–5. (e) Saturation magnetization and coercivity of Mg-3. (f) Cole–Cole curve of Mg-3. (g) Loss tangents of Mg-3. (h) Comparison of absorption performance with that of other materials.

frequency-dependent attenuation trend (Fig. S8 in the ESM). This behavior originates from the relaxation hysteresis effect of dipoles in response to an externally applied alternating electric field, which directly induces dielectric loss. The ε' value of Mg-3 exhibits an opposite trend, which is attributed to phase differences among the different samples. Comparative analysis (Fig. S8 in the ESM) reveals that the ε' value of Mg-3 is between those of the other samples, which is attributed primarily to its distinct defect engineering regulation. In a high-entropy ceramic lattice system, differences in the electronic configurations of multivalent cations lead to the formation of abundant defects. Specifically, lattice distortion-induced metal vacancies lead to the accumulation of dipoles; an increase in surface V_{OS} concentration significantly reduces the band-gap width, facilitating the generation of localized electron–hole pairs by charging compensation mechanisms, whereas the synergistic effect of surface V_{OS} and lattice distortions further enhances polarization loss. Additionally, the multiphase structural characteristics of the material further amplify the polarization effect. Notably, the heterointerface between the CuO phase and the $(Fe_{0.5}Mg_{0.5}CoNiCuMn)_3O_4$ phase results in significant space charge accumulation, resulting in interfacial polarization.

The frequency response characteristics of the imaginary permittivity (ε'') indicate that ε'' for Mg-3 tends to monotonically increase with increasing frequency, confirming its excellent broadband loss capability. Typically, ε'' is governed by both polarization loss and conductive loss. To further quantify their respective contributions, ε'' can be decomposed into corresponding components using Eqs. (S3)–(S5) in the ESM) in the ESM [33].

Figure S9 in the ESM shows the variation trends of ε_c'' and ε_p'' in the Mg-1–5 systems, which are derived from conductivity measurements and theoretical calculations. The conductivity evolution (Fig. 4(c)) reveals an initial increase followed by a decrease with increasing Mg content, where Mg-3 exhibits the highest conductivity of 0.39 $S{\cdot}m^{-1}$, whereas Mg-5 has a conductivity of only 0.31 $S{\cdot}m^{-1}$. This phenomenon can be attributed to the electron injection effect: The appropriate incorporation of Mg optimizes the band structure and carrier concentration, forming a three-dimensional (3D) conductive network that enhances electron mobility. However, when the Mg concentration exceeds a critical value, the space-charge shielding effect becomes dominant, leading to a decrease in conductivity. This occurs due to excessive carrier accumulation at the grain boundaries, which hinders long-range charge transport. Quantitative analysis reveals that for Mg-1–5, the variation in conductive loss follows the same trend as that of conductivity; therefore, Mg-3 exhibits the maximum ε_c'' value. Moreover, the value of ε_c'' is smaller than that of ε_p'', and polarization loss remains the dominant mechanism. Therefore, the dielectric loss mechanism of the synthesized Mg-1–5 materials is governed primarily by polarization loss. In summary, the dielectric loss in the Mg-3 system is governed primarily by interfacial polarization, dipole polarization, and conductive loss, with polarization loss playing a dominant role. The presence of a Cole circle also confirms this (Fig. 4(f)).

The exceptional microwave absorption properties of a material are closely linked to its magnetic loss. To investigate the influence of the Mg concentration on the magnetic properties of the Mg-1–5 systems, magnetic hysteresis loops are measured at room temperature over a field range from −20,000 to 20,000 Oe (Fig. 4(d)). All the samples exhibit similar hysteresis loop shapes, characterized by narrow loops, indicative of typical soft magnetic properties. Figure 4(e) presents the variation trends of the magnetization and coercivity. As the Mg concentration increases, the saturation magnetization (M_s) and coercivity (H_c) tend to decrease.

Figure 4(b) shows the frequency-dependent variations in the real (μ') and imaginary (μ'') components of the permeability for Mg-3. The results indicate that both μ' and μ'' exhibit a decreasing trend with increasing frequency, with a resonance peak appearing in the lower frequency region. This phenomenon arises from the coupling effect between the magnetic moment precession frequency and the impressed electromagnetic field frequency. When the resonance conditions are met, significant damping loss is induced, confirming the presence of natural resonance in the Mg-3 system. In addition to natural resonance, magnetic loss mechanisms also include domain wall resonance, magnetic hysteretic loss, and eddy current loss. Among these, domain wall resonance and magnetic hysteretic loss primarily occur in the megahertz range and are not the focus of this study. Eddy current loss originates from induced currents generated within a sample under an alternating electromagnetic field and is typically evaluated using the eddy current loss factor (C_0). As shown in Fig. S10 in the ESM, the nearly linear C_0–f curve demonstrates the dominant role of eddy current loss within the magnetic loss mechanisms. Furthermore, a comparative analysis of the dielectric loss tangent ($\tan\delta_\varepsilon$) and magnetic loss tangent ($\tan\delta_\mu$) reveals that the loss mechanism of Mg-3 exhibits significant frequency-dependent characteristics. Overall, across the entire X-band, both dielectric loss and magnetic loss mechanisms coexist in the material. However, owing to its low saturation magnetization, dielectric loss predominates in most frequency regions. Notably, a distinct natural resonance peak appears within the range of 9.5–10.5 GHz (Fig. 4(b)). This resonance effect synergizes with eddy current loss, collectively enhancing the magnetic loss capability of the material. Consequently, within this specific frequency range, magnetic loss becomes the dominant mechanism (Fig. 4(g)).

From a macroscopic perspective, impedance matching (Z_{in}/Z_0, Z_{in} and Z_0 represent the input impedance and intrinsic impedance, respectively) and the attenuation constant (α) are two key parameters for evaluating the electromagnetic wave-absorption performance of materials [34].Impedance matching reflects the material's ability to store and transmit incident electromagnetic waves, with optimal impedance matching facilitating effective absorption. By solving the relevant equations, impedance matching analysis reveals that for a matching thickness of 2.3 mm (Fig. S11 in the ESM), the normalized impedance values of the Mg-1–5 systems fall within the theoretically ideal range (0.52–1.9), indicating excellent impedance matching characteristics (Eq. (1)).

$$\mathrm{RL} = 20\log\left|(Z_{in} - Z_0)/(Z_{in} + Z_0)\right| \leq -10 \qquad (1)$$

This behavior is attributed primarily to the synergistic regulation of the dielectric constant and magnetic permeability, which enables effective electromagnetic parameter matching. The attenuation constant quantifies the material's ability to dissipate electromagnetic wave energy, with higher values corresponding to stronger attenuation capabilities.

As shown in Fig. S12 in the ESM, the evolution of α exhibits a nonmonotonic trend with increasing Mg doping concentration, initially increasing but then decreasing. Notably, the Mg-3 system achieves the highest α value, suggesting superior electromagnetic wave attenuation performance within this system. Therefore, compared with other microwave absorption materials (Fig. 4(h)) and Table S4 in the ESM, the rational design of impedance matching and attenuation optimization based on defect

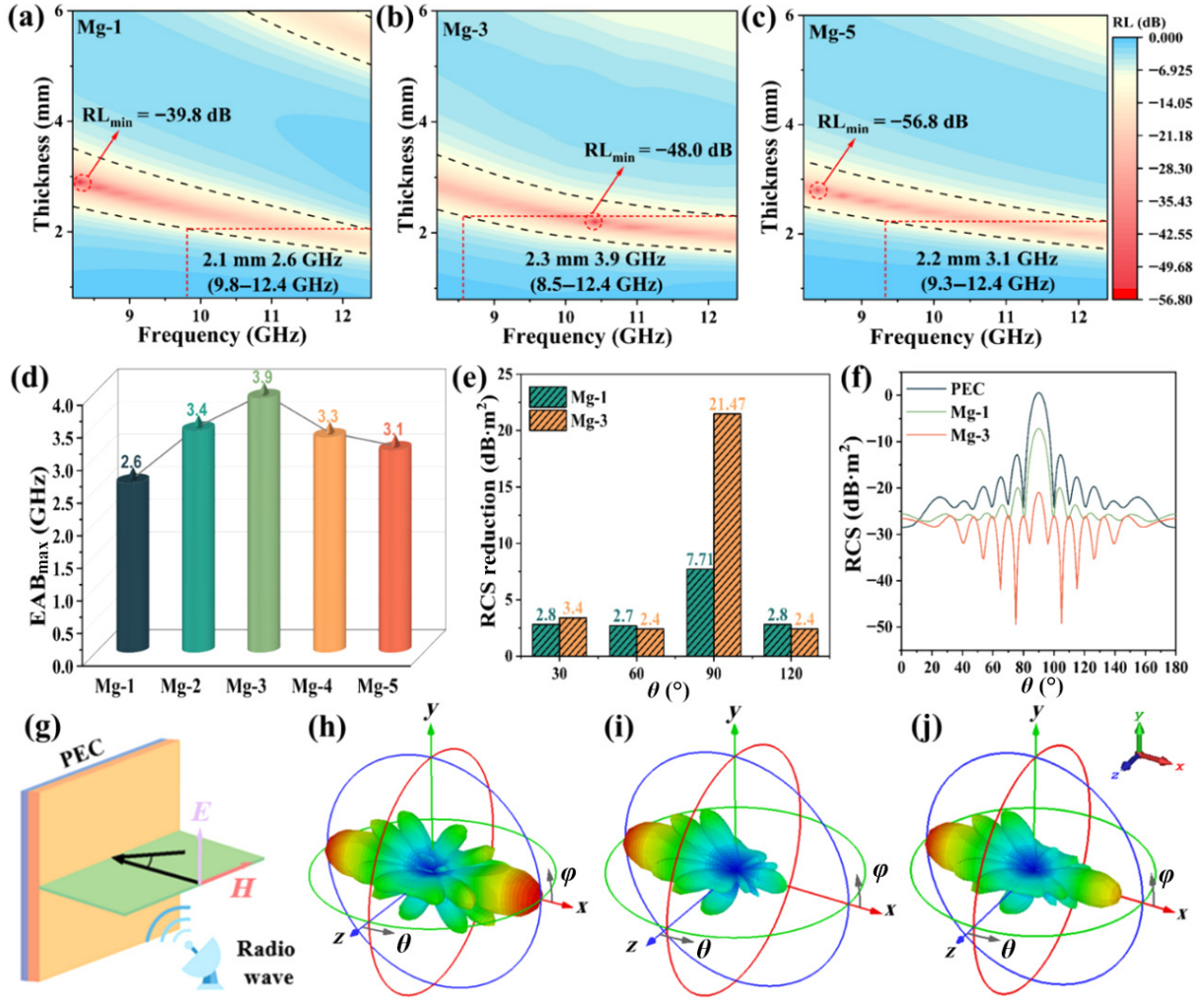

Fig. 5 (a–c) Two-dimensional contour plots of reflection loss for Mg-1–5 in range of 8.2–12.4 GHz. (d) EAB_{max} values of Mg-1–5. (e, f) RCS values. (g) RCS simulation. (h–j) 3D radar scattering simulation results of PEC, Mg-1, and Mg-3.

engineering effectively enhances electromagnetic wave absorption [35–37].

Figures 5(a)–5(d) show the variations in RL_{min} and EAB_{max} for the Mg-1–5 systems. The experimental results demonstrate that all the samples exhibit excellent electromagnetic wave absorption performance, with EAB_{max} values exceeding 2.6 GHz and RL_{min} values better than −25.8 dB for thicknesses below 2.3 mm. Notably, the electromagnetic wave-absorption capability first increases but then decreases nonlinearly with increasing Mg doping concentration. Specifically, at a thickness of 2.1 mm, Mg-1 achieves an EAB_{max} of 2.6 GHz, whereas Mg-3 exhibits an EAB_{max} of 3.9 GHz at 2.3 mm, virtually covering the X-band (8.2–12.4 GHz). When the thickness is further decreased to 2.2 mm, Mg-3 attains an exceptional RL_{min} of −48 dB, indicating superior wave absorption capability. At a thickness of 2.8 mm, Mg-5 achieves an exceptional RL_{min} of −56.8 dB.

Previous studies have highlighted the critical roles of lattice distortion and surface V_{OS} in electromagnetic wave attenuation. In this work, we find that both the degree of lattice distortion and the surface V_{OS} concentration exhibit a parabolic trend, initially increasing and then decreasing, whereas RL_{min} and EAB_{max} exhibit similar phenomena. This behavior can be attributed to a synergistic defect effect. A moderate degree of lattice distortion enhances polarization loss by introducing metal vacancies and strengthening dipole polarization effects. Nevertheless, excessive distortion can lead to elemental segregation, impeding electron conduction pathways and degrading the overall conductive network. Similarly, the introduction of surface V_{OS} lowers the electron transition barrier, facilitating electron hopping and transport. Additionally, moderate surface V_{OS} concentrations serve as polarization centers, enhancing dielectric loss via dipole polarization. However, excessive surface V_{OS} may induce local defect overload, disrupting the lattice integrity and consequently reducing dielectric loss. Therefore, optimizing defect engineering requires a dynamic balance between the surface V_{OS} concentration and the degree of lattice distortion. When the Mg/Fe molar ratio is optimized to 1 : 1 (lattice distortion degree: 0.86%, surface V_{OS} concentration: 51.89%), a synergistic enhancement effect is achieved, resulting in the optimal electromagnetic wave absorption performance.

To evaluate the electromagnetic loss characteristics of Mg-1–5 under far-field conditions, a composite structural model comprising a PEC substrate and an absorbing layer is established using the CST electromagnetic simulation platform (Fig. 5(g)) [38]. The angular-domain response of its RCS is systematically analyzed [38]. The simulation results demonstrate that, compared with conventional metallic backing, the Mg-3 composite material exhibits superior RCS suppression across the 0°–180° incidence range, with reflection intensities consistently below −20 dB·m². Notably, at normal incidence (90°), the RCS value of Mg-3 is

reduced by 21.47 dB·m² relative to that of the metallic reference (Figs. 5(e)–5(j)), highlighting its exceptional capability for broadband and wide-angle electromagnetic wave manipulation.

3.3 Microwave absorption properties after high-temperature oxidation

To evaluate the high-temperature oxidation resistance of the material, the sintered Mg-3 sample is subjected to gradient oxidation treatments at temperatures ranging from 800 to 1200 °C (in increments of 100 °C) for 2 h in an air atmosphere, which are subsequently designated Mg-6–10. XRD analysis (Fig. 6(a)) reveals that the diffraction peaks of the oxidized samples remain highly consistent with those of the unoxidized material, with no observable shifts in the crystallographic indices of the $(Fe_{0.5}Mg_{0.5}CoNiCuMn)_3O_4$ phase and CuO phase, indicating excellent phase stability under high-temperature oxidation conditions. The key regulatory effect of internal defects on the microwave absorption performance is systematically investigated. To characterize the evolution of the lattice distortion and surface V_{OS} concentration quantitatively, a comprehensive analysis of the Mg-10 sample is conducted using Rietveld refinement in conjunction with high-resolution O 1s XPS spectra (Figs. 6(b) and 6(c), Table S1 and Table S3 in the ESM). The experimental results indicate that, compared with that of the Mg-3 sample, the surface V_{OS} concentration of Mg-10 is significantly reduced, with values even lower than those of the Mg-1 reference sample.

Analysis of the evolution of the electromagnetic parameters (Figs. 6(d)–6(g)) reveals that both ε' and ε'' significantly increase, which is attributed primarily to the enhanced dielectric polarization capability resulting from the reduced defect concentration. Simultaneously, μ' increases while μ'' decreases, with μ'' consistently exhibiting negative values across the entire X-band frequency range. This suggests that the radiation effect induced by charge motion dissipates magnetic energy, thereby weakening the magnetic loss mechanism. Additionally, a mutation occurs at 10 GHz, which is typically associated with the dispersion characteristics of ferrite materials at their resonance frequency, originating from the relaxation lag response of dipoles to the externally applied alternating electric field. Notably, C_0 remains on a straight line, confirming the existence of eddy current loss. A comparative analysis of $\tan\delta_\varepsilon$ and $\tan\delta_\mu$ further indicates that dielectric loss is the primary contributor to electromagnetic wave attenuation. However, in comparison with the Mg-3 sample, the Mg-10 exhibits increased $\tan\delta_\varepsilon$ alongside reduced $\tan\delta_\mu$, directly leading to the deterioration of its impedance matching and a

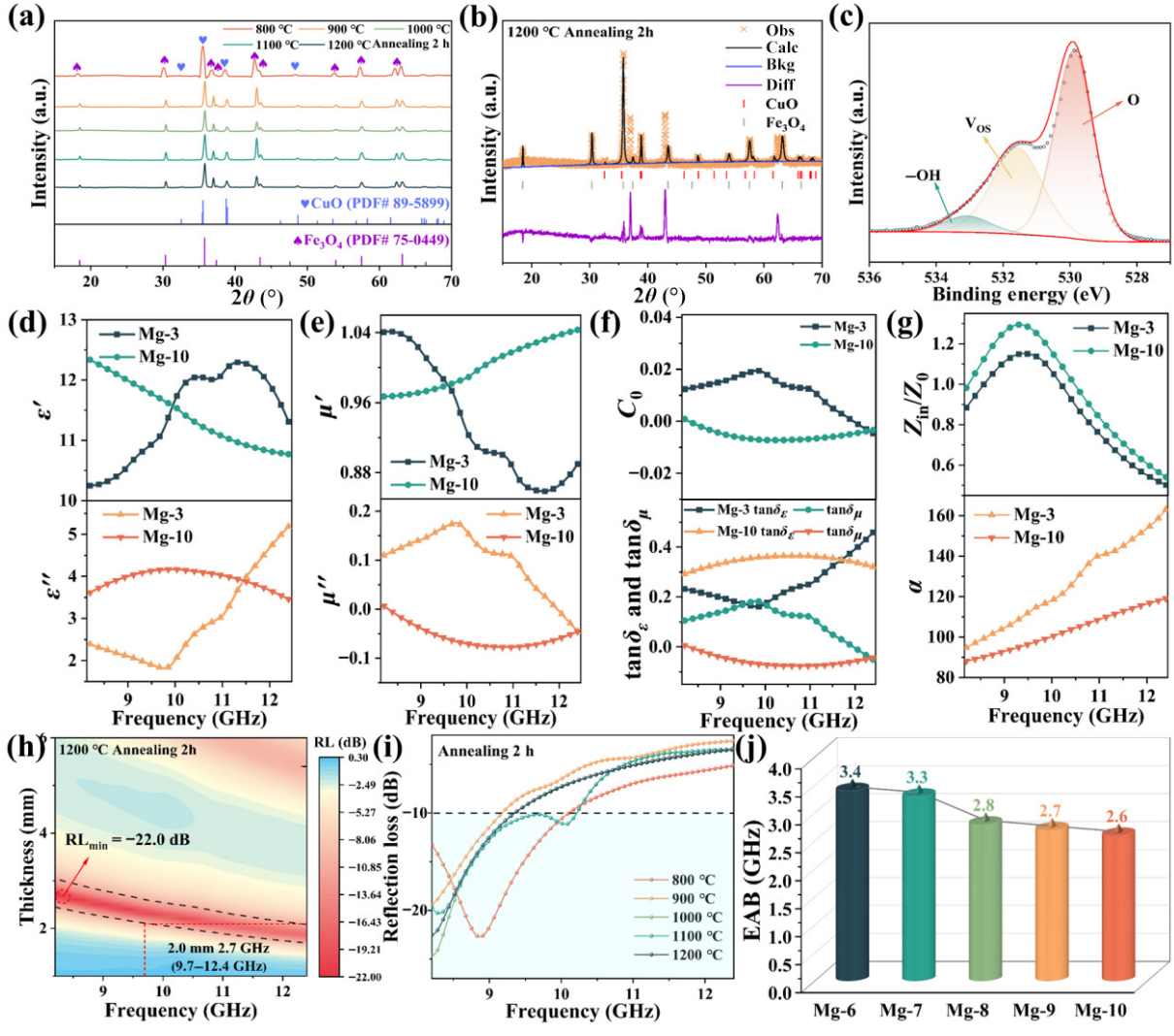

Fig. 6 (a) XRD patterns of Mg-6–10. (b, c) Rietveld refinement and high-resolution XPS spectra of Mg-10. (d, e) Electromagnetic parameters of Mg-3 and Mg-10. (f, g) Eddy current loss factor, loss tangent, impedance matching, and attenuation constant of Mg-3 and Mg-10. (h–j) Minimal reflection loss and maximum effective absorption band of Mg-6–10.

decline in the attenuation constant. Comprehensive experimental analysis indicates that the oxidation process leads to the degradation of wave-absorption performance through the synergistic effects of structural densification and the annihilation of surface oxygen vacancies. These effects operate at both the macroscopic level of grain growth and the microscopic level of depletion of charge carriers and polarization centers, collectively impairing the material's polarization loss and conductive loss. A detailed explanation is provided as follows: First, structural densification serves as the initial stage of performance degradation. As shown in Fig. S13 in the ESM, the oxidized sample exhibits significant grain coarsening, a more densely sintered morphology, and a clear reduction in porosity. This structural evolution induces two major effects: (i) Densification markedly reduces the density of interfacial defects such as grain boundaries, thereby weakening the contribution of interfacial polarization to dielectric loss. (ii) A more structurally continuous process allows charge transport pathways to become "smoother", which in turn reduces the scattering of charge carriers during transmission—which is unfavorable for the effective dissipation of electromagnetic wave energy. Second, the annihilation of surface oxygen vacancies is the direct cause of the sharp decline in both the conduction and polarization capabilities. XPS analysis confirms a noticeable decrease in the concentration of surface oxygen vacancies after oxidation. As crucial charged point defects and polarization centers, the reduction in surface oxygen vacancy concentration triggers a chain of effects: In terms of electrical conductivity, surface oxygen vacancies are key sources of free charge carriers; their annihilation directly leads to a decrease in the charge carrier concentration. More importantly, the decreased concentration of surface oxygen vacancies disrupts the original conductive network, resulting in a decrease in electrical conductivity. In terms of polarization relaxation, surface oxygen vacancies act as dipoles that can generate dipole polarization under an alternating electric field. Their extensive depletion significantly weakens this vital polarization mechanism, thereby reducing the material's dielectric loss capability.

The two-dimensional (2D) reflection loss and effective absorption bandwidth results (Figs. 6(h)–6(j)) indicate that oxidation treatment leads to a decreasing trend in both the minimum reflection loss and the maximum effective absorption bandwidth, with the degree of performance degradation intensifying as the oxidation temperature increases. Notably, after oxidation at 1200 °C, the EAB_{max} in the X-band sharply decreases to 2.7 GHz, representing an approximately 30% reduction compared with that of the unoxidized sample.

3.4 Mechanism of enhanced electromagnetic wave absorption

The mechanism of electromagnetic wave absorption of Mg-1–10 is illustrated in Fig. 7. When electromagnetic waves impinge on the material surface, a portion is reflected, whereas the remaining portion penetrates into the material and is effectively attenuated through dielectric loss and magnetic loss mechanisms. This performance is due primarily to the following three mechanisms [39–42]:

First, structure-induced interfacial polarization: A heterogeneous structure is formed in Mg-1–10, consisting of a bottom $(Fe_{0.5}Mg_{0.5}CoNiCuMn)_3O_4$ phase and strip-distributed CuO phases. This structure effectively promotes the interfacial polarization process [43].

Second, defect engineering-enhanced dielectric loss: Through precise regulation of the defect concentration gradient, defect engineering plays a key role in optimizing various dielectric loss mechanisms, including dipole polarization, interfacial polarization, and conduction polarization, specifically manifested as follows [44–46]:

(1) Lattice distortion modulation: The significant radius differences among multiple principal ions (Fe, Mg, Co, Ni, Cu, and Mn) induce strong local stress fields, leading to notable lattice distortions and thereby facilitating the formation of metal vacancies. These vacancies act as high-density defect dipoles, enhancing the dipole polarization response.

(2) Dual role of surface oxygen vacancies: Surface oxygen vacancies with varying concentrations are introduced through the Fe/Mg composition design. Under an alternating electric field, surface oxygen vacancies serve as polarization centers, forming defect-induced dipoles by trapping and releasing carriers, thereby enhancing polarization loss. Simultaneously, intrinsic surface oxygen vacancies introduce defect levels within the band gap, reducing the energy barrier for electron transitions and promoting electron hopping, thus improving conduction loss.

(3) Synergistic effect of interfacial defects: Grain boundaries and discontinuous lattice fringes generated in Mg-1–10 act as polarization centers, causing interfacial charge redistribution and generating additional dipole moments, synergistically enhancing polarization loss and further improving the electromagnetic wave-absorption capability.

Third, synergistic magnetic loss mechanism: Multivalent cations (e.g., Fe^{2+}/Fe^{3+}) occupy different lattice sites, regulating the arrangement of spin magnetic moments through superexchange interactions and inducing magnetic loss under an alternating magnetic field. Notably, in this spinel/rock-salt composite system, the constrained electrical conductivity allows eddy current loss to replace natural resonance as the dominant magnetic mechanism. This conductivity constraint further optimizes the magnetic loss process, endowing the material with excellent microwave absorption performance.

Ultimately, by precisely regulating the Fe/Mg ratio, combined with dual-phase structure design and defect engineering, synergistic control of the lattice distortion and surface oxygen vacancy concentration is achieved. This effectively tunes the dielectric and magnetic loss characteristics of the material, optimizing its electromagnetic wave absorption performance.

3.5 Thermal transport properties of high-entropy ceramics

To meet the increasing demand for multifunctional materials in aerospace thermal management applications, this study systematically evaluates the thermal transport properties of Mg-1–5 (Figs. 8(a)–8(c)). The results reveal that as the Mg content increases, a three-dimensional thermal conduction network is progressively formed, leading to a significant increase in both the thermal conductivity (α) and the thermal diffusivity (k). Among the investigated samples, Mg-5 exhibits an outstanding thermal conductivity of 2.154 $W{\cdot}m^{-1}{\cdot}K^{-1}$, surpassing typical thermally conductive microwave absorbing materials such as $SiBCN/SiBCN_{nf}$, BN@C, CNTs@PEG, $BN_{0.66}/Ni_{0.33}/CNT_7$/WPU, and r-GO@$Fe_3O_4$ [47–50]. Furthermore, the strong positive correlation between the thermal conductivity and thermal diffusivity (Eq. (S7) in the ESM) further validates the synergistic enhancement of the thermal transport properties induced by the three-dimensional thermal conduction network. The observed thermal conductivity is governed by the synergistic effect of two primary mechanisms: phonon conduction and ion conduction [51]. Phonon conduction serves as the dominant mechanism establishing the thermal conductivity, whereas ion conduction provides an additional contribution that further enhances its value. Specifically, the characteristic "long-range disorder and

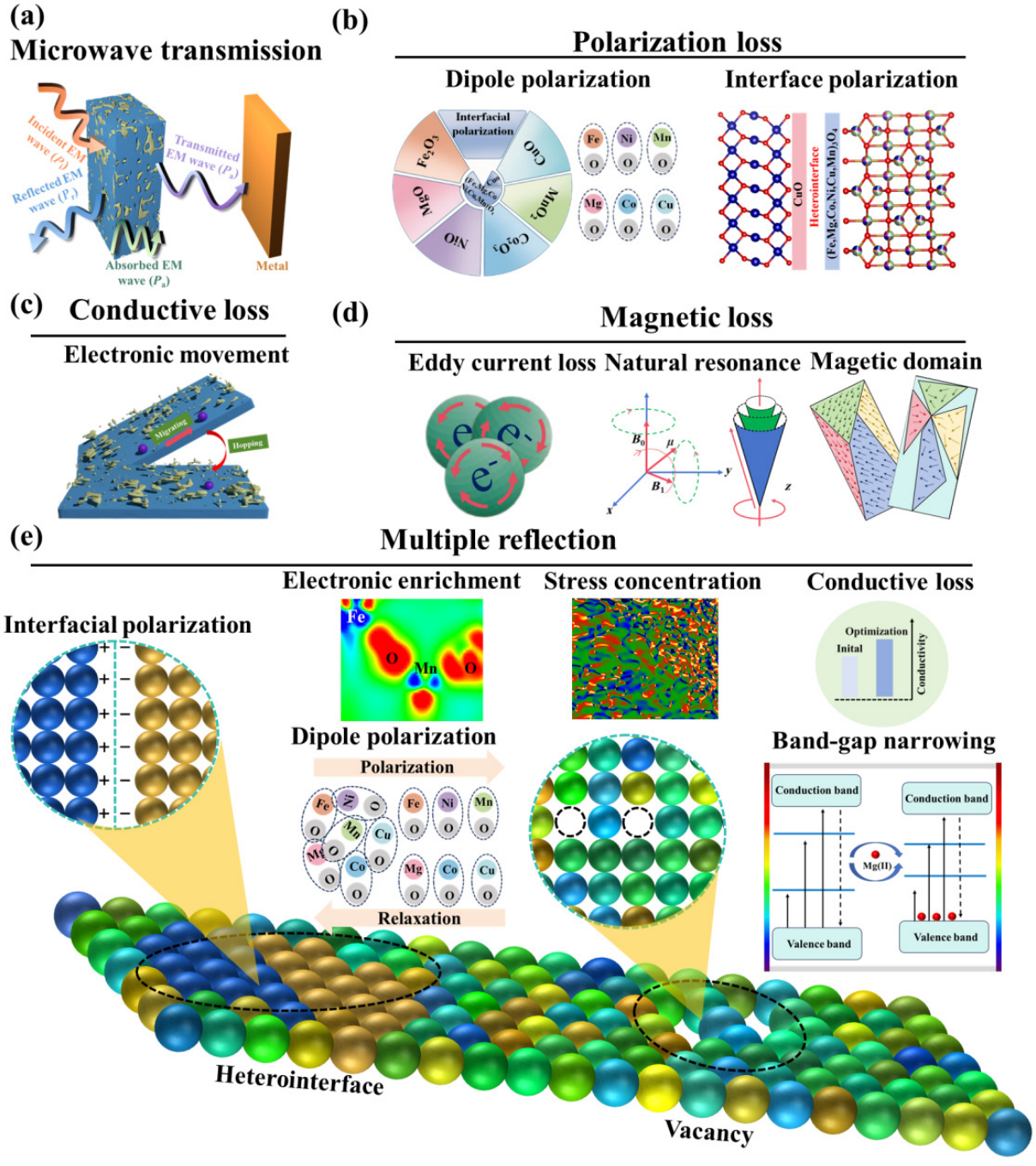

Fig. 7 Electromagnetic wave-absorption mechanism of Mg-1–10.

short-range order" structure of the high-entropy system leads to internal momentum balance within the framework of the dual-phonon scattering model, which is key to its intrinsic thermal conductivity [52]. From the perspective of ion transport, variations in the Mg^{2+} concentration induce changes in the concentration of internal defects, such as surface oxygen vacancies and lattice defects. These defects provide numerous low-energy-barrier pathways for rapid Mg^{2+} hopping, thereby enhancing the contribution of ion transport to the overall thermal conductivity.

From the standpoint of practical application requirements, traditional functional fillers often face the limitation of serving a single purpose. For example, although high-thermal-conductivity fillers such as aluminum nitride significantly increase the thermal conductivity of composite materials, their inherent electromagnetic properties result in a general lack of wave-absorption ability. On the other hand, most carbon materials used for wave absorption exhibit low degrees of graphitization and, consequently, poor thermal conductivity [53]. In contrast, the high-entropy material developed in this study demonstrates unique comprehensive advantages. Its thermal conductivity of 2.154 $W \cdot m^{-1} \cdot K^{-1}$ not only far exceeds that of traditional wave-absorbing fillers but also, through defect engineering and dual-phase regulation, equips it with considerable electromagnetic wave dissipation capability. This enables a single filler to synergistically perform the dual functions of "wave absorption" and "thermal conduction".

To further validate the thermal transport capability of the Mg-1–5 composite, a thermal transport experimental system was established. During the experiment, samples (diameter: 11.0 mm, thickness: 1.5 mm) are placed on a heating platform and subjected

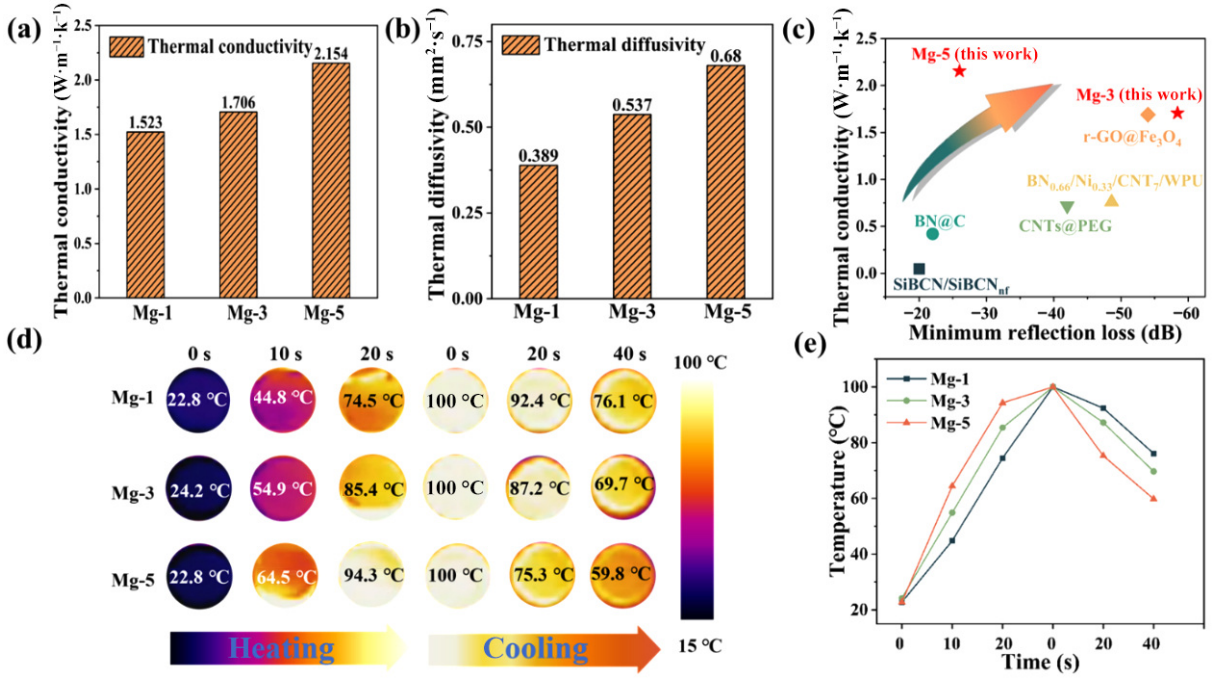

Fig. 8 (a, b) Thermal conductivity and thermal diffusivity of Mg-1–5. (c) Heat conductivity comparison of wave-absorbing materials from previous reports. (d, e) Infrared thermal images and heating/cooling time curves of Mg-1–5.

to continuous heating at 100 °C for 60 s. A thermal infrared imaging system is employed to monitor the spatiotemporal evolution of the surface temperature distribution in real time (Figs. 8(d) and 8(e)). The experimental results reveal that all the Mg-1–5 samples exhibit a typical radial heat conduction pattern, with Mg-5 demonstrating the best heat transfer dynamics. Specifically, its thermal disturbance front propagates from the edge to the center within 20 s, indicating an increase in heat transfer efficiency compared with that of Mg-1.

4 Conclusions

In summary, a defect-engineering-driven dual-phase strategy was successfully implemented to design $(Fe_{0.5}Mg_{0.5}CoNiCuMn)_3O_4$@CuO composite ceramics with tunable microwave absorption. The lattice distortion and surface oxygen vacancy concentration were positively correlated with the absorption performance. The optimized material exhibited a minimum reflection loss of −48 dB and an effective absorption bandwidth of 3.9 GHz in the X-band, attributed to the frequency-dependent synergistic effect between the dielectric and magnetic loss mechanisms. Moreover, the ceramic demonstrated remarkable structural and functional stability, retaining 70% of its absorption bandwidth after oxidation at 1200 °C, along with a thermal conductivity of 2.154 $W \cdot m^{-1} \cdot K^{-1}$. This work provides an effective defect-mediated approach for developing high-performance electromagnetic absorbing materials with integrated temperature resistance and thermal stability.

Acknowledgements

This work was supported by the National Natural Science Foundation of China (Nos. 12374394 and 52402362), the Youth Project of Natural Science Foundation of Jiangsu Province (No. BK20230341), Nanjing Overseas Educated Personnel Science and Technology Innovation Program, the "Qinglan Project" Young, Middle-aged Academic Leaders Program of Jiangsu Province, and the Priority Academic Program Development of Jiangsu Higher Education Institutions (PAPD).

Availability of data and materials

The data that support the findings of this study are available from the corresponding author upon reasonable request.

Competing interests

The authors have no competing interests to declare that are relevant to the content of this article.

Electronic Supplementary Material

Supplementary material is available in the online version of this article at https://doi.org/10.26599/JAC.2025.9221229.

References

[1] Wang ZX, Ma L, Ma HY, *et al.* Double-layer electromagnetic shielding materials with microcellular structure for strong absorption and low reflection. *J Mater Sci Technol* 2026, **245**: 227–237.

[2] Sun RL, Ming XR, Yan GL, *et al.* Efficient nanofibrous electromagnetic wave absorber inspired by spider silk hunting. *Small* 2024, **20**: 2407178.

[3] Cai B, Zhou L, Zhao PY, *et al.* Interface-induced dual-pinning mechanism enhances low-frequency electromagnetic wave loss. *Nat Commun* 2024, **15**: 3299.

[4] Liu TT, Zheng Q, Cao WQ, *et al. In situ* atomic reconstruction engineering modulating graphene-like MXene-based multifunctional electromagnetic devices covering multi-spectrum. *Nano-Micro Lett* 2024, **16**: 173.

[5] Zhang XC, Zhang M, Wang MQ, *et al.* Metal single-atoms toward electromagnetic wave-absorbing materials: Insights and perspective. *Adv Funct Mater* 2024, **34**: 2405972.

[6] Yu SW, Wang CC, Chen ZZ, *et al.* Additive manufacturing of broadband electromagnetic wave absorbing materials: Polymer-derived SiC/Si_3N_4 composites with triply periodic minimal surface meta-structure. *Chem Eng J* 2024, **483**: 149185.

[7] Ren B, Deng YM, Jia YJ, *et al.* Electromagnetic wave absorbing ceramics composites made of polymer-derived SiC with BN@CNTs pyrolyzed higher than 1200 °C. *J Mater Sci Technol* 2023, **167**: 213–227.

[8] Qian JJ, Ma DD, Zhou XL, *et al.* Synthesis of SiOC@C ceramic nanospheres with tunable electromagnetic wave absorption performance. *J Adv Ceram* 2024, **13**: 1394–1408.
[9] Gao H, Qin L, Tao SF, *et al.* Multiple tuned carbon nanotubes by rare earth oxides for high-efficiency electromagnetic wave absorption. *Adv Compos Hybrid Ma* 2024, **7**: 135.
[10] Yang JC, Wen QB, Feng B, *et al.* Microstructural evolution and electromagnetic wave absorbing performance of single-source-precursor-synthesized SiCuCN-based ceramic nanocomposites. *J Adv Ceram* 2023, **12**: 1299–1316.
[11] Lei CK, Ding DH, Xiao GQ, *et al.* Electromagnetic wave absorbing properties and oxidation resistance of CNTs/SiC composite bonded with CNTs@calcium aluminate cement. *Ceram Int* 2024, **50**: 35007–35018.
[12] Zhou YC, Zhao B, Chen H, *et al.* Electromagnetic wave absorbing properties of TMCs (TM=Ti, Zr, Hf, Nb and Ta) and high entropy $(Ti_{0.2}Zr_{0.2}Hf_{0.2}Nb_{0.2}Ta_{0.2})C$. *J Mater Sci Technol* 2021, **74**: 105–118.
[13] Liu CC, Chen QY, Sun P, *et al.* Synthesis of novel high-entropy diborides with high-efficiency electromagnetic wave absorption and excellent thermal stability. *J Adv Ceram* 2025, **14**: 9221030.
[14] Zhu YJ, Guan L, Duan CQ, *et al.* High-entropy transition metal carbide nanowires with enhanced microwave absorption properties. *J Mater Sci Technol* 2025, **224**: 302–311.
[15] Zhao B, Du YQ, Yan ZK, *et al.* Structural defects in phase-regulated high-entropy oxides toward superior microwave absorption properties. *Adv Funct Mater* 2023, **33**: 2209924.
[16] Zhu M, Cao JC, Chen XN, *et al.* Synthesis and thermoelectric properties of a new high-entropy spinel ferrite $(Mn_{0.2}Co_{0.2}Cu_{0.2}Zn_{0.2}Mo_{0.2})Fe_2O_4$. *Ceram Int* 2024, **50**: 55589–55597.
[17] Ma JB, Zhao B, Xiang HM, *et al.* High-entropy spinel ferrites MFe_2O_4 (M = Mg, Mn, Fe, Co, Ni, Cu, Zn) with tunable electromagnetic properties and strong microwave absorption. *J Adv Ceram* 2022, **11**: 754–768.
[18] Li WY, Li F, Qiu XM, *et al.* Broadband electromagnetic wave attenuation in high-entropy $La(Cr_{0.2}Mn_{0.2}Fe_{0.2}Co_{0.2}Ni_{0.2})O_3$: Engineering bond properties via configurational entropy. *Ceram Int* 2025, **51**: 31503–31512.
[19] Gan K, Cai C, Zong CW, *et al.* Preparation and properties of Sr $(CrMnFeCoNi)_3O_4$ and $Sr(MgAlTiCrFe)_{12}O_{19}$ high entropy strontium ferrite systems and valance state analysis. *Ceram Int* 2022, **48**: 23963–23974.
[20] Pang HF, Duan YP, Huang LX, *et al.* Research advances in composition, structure and mechanisms of microwave absorbing materials. *Compos Part B—Eng* 2021, **224**: 109173.
[21] Wu LH, Liu J, Liu X, *et al.* Microwave-absorbing foams with adjustable absorption frequency and structural coloration. *Nano Lett* 2024, **24**: 3369–3377.
[22] Gu FC, Wang W, Meng H, *et al.* Lattice distortion boosted exceptional electromagnetic wave absorption in high-entropy diborides. *Matter* 2025, **8**: 102004.
[23] Liu A, Xu XS, Qiu H, *et al.* Bioinspired hollow heterostructure fillers for enhanced electromagnetic interference shielding in polyimide aerogels. *InfoMat* 2025, **7**: 70060.
[24] Wang T, Zhao WX, Miao YK, *et al.* Enhancing defect-induced dipole polarization strategy of $SiC@MoO_3$ nanocomposite towards electromagnetic wave absorption. *Nano-Micro Lett* 2024, **16**: 273.
[25] Yang WT, Han Z, Zheng GP. The influences of lattice distortion on the antiferroelectric transition and relaxation of oxygen vacancies in high-entropy perovskites $(Bi_{0.2}Na_{0.2}Ba_{0.2}K_{0.2}X_{0.2})TiO_3$ with X = Ca, Sr or La. *Scripta Mater* 2021, **203**: 114096.
[26] Xiang HM, Xing Y, Dai FZ, *et al.* High-entropy ceramics: Present status, challenges, and a look forward. *J Adv Ceram* 2021, **10**: 385–441.
[27] Zhang WM, Zhao B, Xiang HM, *et al.* One-step synthesis and electromagnetic absorption properties of high entropy rare earth hexaborides (HE REB_6) and high entropy rare earth hexaborides/borates (HE REB_6/HE $REBO_3$) composite powders. *J Adv Ceram* 2021, **10**: 62–77.
[28] Chen DQ, Zhu XW, Xiong SY, *et al.* Tunable microwave dielectric properties in rare-earth niobates via a high-entropy configuration strategy to induce ferroelastic phase transition. *ACS Appl Mater Inter* 2023, **15**: 52776–52787.
[29] Dai GH, Deng RX, Zhang T, *et al.* Quantitative evaluation of loss capability for *in situ* conductive phase enhanced microwave absorption of high-entropy transition metal oxides. *Adv Funct Mater* 2022, **32**: 2205325.
[30] Yu ZX, Yao ZP, Zhang N, *et al.* Polarization enhanced multi-grain-boundary dendritic micro–nano structure α-Fe for electromagnetic absorption applications: Synthesis and characterization. *RSC Adv* 2015, **5**: 25266–25272.
[31] Zhang BX, Jing QH, Yan SQ, *et al.* Electron irradiation modified point defects of SiC nanoparticles with tunable high electromagnetic wave absorption. *Carbon* 2024, **218**: 118727.
[32] Zhang WM, Zhao B, Ni N, *et al.* High entropy rare earth hexaborides /tetraborides (HE REB_6/HE REB_4) composite powders with enhanced electromagnetic wave absorption performance. *J Mater Sci Technol* 2021, **87**: 155–166.
[33] Yadav RS, Kuřitka I. Recent advances on outstanding microwave absorption and electromagnetic interference shielding nanocomposites of ZnO semiconductor. *Adv Colloid Interfac* 2024, **326**: 103137.
[34] Gai LX, Wang YH, Wan P, *et al.* Compositional and hollow engineering of silicon carbide/carbon microspheres as high-performance microwave absorbing materials with good environmental tolerance. *Nano-Micro Lett* 2024, **16**: 167.
[35] Zeng XJ, Peng XW, Ning Y, *et al.* 3D multifunctional porous pine carbon aerogels coupled with highly dispersed CoFe nanoparticles for robust electromagnetic wave response. *J Mater Sci Technol* 2024, **192**: 6–18.
[36] Zhou W, Yin RM, Long L, *et al.* Enhanced high-temperature dielectric properties and microwave absorption of SiC nanofibers modified Si_3N_4 ceramics within the gigahertz range. *Ceram Int* 2018, **44**: 12301–12307.
[37] Kong L, Yin XW, Li Q, *et al.* High-temperature electromagnetic wave absorption properties of ZnO/$ZrSiO_4$ composite ceramics. *J Am Ceram Soc* 2013, **96**: 2211–2217.
[38] Gao ZG, Iqbal A, Hassan T, *et al.* Tailoring built-in electric field in a self-assembled zeolitic imidazolate framework/MXene nanocomposites for microwave absorption. *Adv Mater* 2024, **36**: 2311411.
[39] Liu TT, Li LY, Gao P, *et al.* High-entropy electromagnetic functional materials: From electromagnetic genes to materials design. *Mat Sci Eng R* 2025, **164**: 100982.
[40] Xie AM, Guo RH, Wu LP, *et al.* Anion-substitution interfacial engineering to construct C@MoS_2 hierarchical nanocomposites for broadband electromagnetic wave absorption. *J Colloid Interf Sci* 2023, **651**: 1–8.
[41] Xie AM, Sheng DH, Liu WL, *et al.* Enhancing electromagnetic absorption performance of molybdate@carbon by metal ion substitution. *J Mater Sci Technol* 2023, **163**: 92–100.
[42] Zhao B, Du YQ, Lv HL, *et al.* Liquid-metal-assisted programmed galvanic engineering of core–shell nanohybrids for microwave absorption. *Adv Funct Mater* 2023, **33**: 2302172.
[43] Zhao B, Yan ZK, Liu LL, *et al.* A liquid-metal-assisted competitive galvanic reaction strategy toward indium/oxide core–shell nanoparticles with enhanced microwave absorption. *Adv Funct Mater* 2024, **34**: 2314008.
[44] Sun H, Che RC, You X, *et al.* Cross-stacking aligned carbon-nanotube films to tune microwave absorption frequencies and increase absorption intensities. *Adv Mater* 2014, **26**: 8120–8125.
[45] Liu QH, Cao Q, Bi H, *et al.* CoNi@SiO_2@TiO_2 and CoNi@air@TiO_2

microspheres with strong wideband microwave absorption. *Adv Mater* 2016, **28**: 486–490.

[46] Du YQ, Yan ZK, You WB, *et al*. Balancing MXene surface termination and interlayer spacing enables superior microwave absorption. *Adv Funct Mater* 2023, **33**: 2301449.

[47] Luo C, Fei DZ, Zhou JT, *et al*. Silver particle-modified BN@C composites for thermal management and microwave absorption. *Ceram Int* 2024, **50**: 22252–22265.

[48] Bai YF, He LL, Lv P, *et al*. Impedance-matched (hydroxylated nano-BN/reduced graphene oxide)@Fe_3O_4/polyaniline composite for efficient microwave absorption and thermal management. *Mater Chem Phys* 2023, **295**: 127193.

[49] Jiang JP, Xue YJ, Li JT, *et al*. Microwave absorption and thermal insulation integrated polymer-derived SiBCN/$SiBCN_{nf}$ ceramic aerogel with enhanced mechanical property. *Ceram Int* 2024, **50**: 41527–41533.

[50] Li ZX, Yang W, Chen Z, *et al*. Boron nitride- and carbon nanotube-bridged interfaces for boosting thermal conduction and electromagnetic wave absorption. *ACS Appl Nano Mater* 2024, **7**: 4264–4276.

[51] Yang YJ, Chen YB, Wang XX, *et al*. Rationally controlling interfaces and oxygen vacancies of CeO_2@C core–shell nanorods/nanofibers for superior microwave absorption and thermal conduction. *Appl Surf Sci* 2024, **665**: 160325.

[52] Luo JW, Lv Z, Zhang LP, *et al*. Modulation of dielectric behavior in ceramic-based materials for integrated electromagnetic waves absorption and thermal conduction. *Adv Funct Mater* 2025, **35**: 2420086.

[53] Xiang ZC, Song Z, Wang TS, *et al*. Bead-like flexible ZIF-67-derived Co@carbon composite nanofibre mat for wideband microwave absorption in C-band. *Carbon* 2024, **216**: 118573.